PERGAMON

International Journal of Heat and Mass Transfer 43 (2000) 297–310

International Journal of HEAT and MASS TRANSFER

www.elsevier.com/locate/ijhmt

Convective instability in a time-dependent buoyancy driven boundary layer

A.M.H. Brooker*, J.C. Patterson, T. Graham, W. Schöpf

Centre for Water Research, The University of Western Australia, Nedlands 6907, Australia

Received 27 May 1998; received in revised form 8 March 1999

Abstract

The stability of the parallel time-dependent boundary layer adjacent to a suddenly heated vertical wall is described. The flow is investigated through experiments in water, through direct numerical simulation and also through linear stability analysis. The full numerical simulation of the flow shows that small perturbations to the wall boundary conditions, that are also present in the experimental study, are responsible for triggering the instability. As a result, oscillatory behaviour in the boundary layer is observed well before the transition to a steady two-dimensional flow begins. The properties of the observed oscillations are compared with those predicted by a linear stability analysis of the unsteady boundary layer using a quasi-stationary assumption and also using non-stationary assumptions by the formulation of parabolized stability equations (PSE).

Keywords: Natural convection; Stability; Unsteady

1. Introduction

An understanding of transient natural convection is of great importance in industrial applications where sudden changes in the surface boundary conditions can cause the heat transfer characteristics of a device to change significantly. Such situations arise for example in cooling systems and in crystal growth procedures. This paper focuses on the transient flow induced by the sudden heating of a vertical plate. Idealised in an infinite flow domain, heat transfer takes place purely by conduction and the one-dimensional form for the Navier–Stokes and energy equations is satisfied. In practice, finite geometry means that the symmetry is broken at the bottom of the heated element. The effect of this leading edge is propagated downstream producing a steady flow with a small vertical temperature gradient and a small horizontal velocity component is present. The analysis by Siegel [1] was the first to describe the behaviour of the leading edge effect in this way. Various experimental studies (summarized by Gebhart et al. [2]) have confirmed this basic flow regime. Other studies have attempted to predict the velocity at which the leading edge signal propagates up through the flow [3–5].

A study by Joshi and Gebhart [6] examined experimentally the breakdown of the one-dimensional flow using a constant heat flux boundary condition on a semi-infinite vertical wall. By making localised measurements of temperature and velocity, they found that the temperature and velocity traces deviated from

* Corresponding author. Current address: British Energy, Barnett Way, Barnwood, Gloucester GL4 3RS, UK. Tel.: +44-1452-652-143.

E-mail address: a.brooker2@ne.british-energy.com (A.M.H. Brooker)

0017-9310/00/$ - see front matter
PII: S0017-9310(99)00127-1

Nomenclature

a_q^S	temporal amplification from Eq. (27)
A	amplitude of the sinusoidal perturbation
A_r	amplitude of the random perturbation
$B(k_0, Gr_t)$	$\int_{Gr_{t_0}}^{Gr_t} \omega_{0i}(G)\,\mathrm{d}G$
g	acceleration due to gravity
Gr_t	$U_0\delta/\nu = g\beta\Delta T\delta^3/\nu^2$
H	cavity height
Pr	ν/κ
R	random value
Ra	$g\beta\Delta T H^3/\nu\kappa$
S^*	heat source
t^*	dimensional time
t_c	t^*H^2/ν
T^*	dimensional temperature
$\bar{T}$	$(T^*-T_0)/\Delta T$
T_h	temperature of the cavity wall
T_0	ambient temperature
$\bar{T}(y, t)$	baseflow temperature fields
$T'(x, y, t)$	perturbations temperature fields
u^*	dimensional vertical velocity
$\bar{u}$	u^*/U_0
U_0	$g\beta\Delta T\delta^2/\nu$
v^*	dimensional horizontal velocity
x^*	dimensional vertical ordinate
x_c	x^*/H
y	y^*/δ
y^*	dimensional horizontal ordinate
y_c	y^*/H

Greek symbols

β	coefficient of thermal expansion
δ	$\sqrt{4\kappa t_0}$
Δt^*	timestep
ΔT	T_h-T_0
η	$y^*/\sqrt{4\kappa t^*}$
κ	the thermal diffusivity
ν	kinematic viscosity
$\bar{\psi}(y, t)$	baseflow streamfunction
$\psi'(x, y, t)$	perturbation streamfunction
$\hat{\omega}(t)$	complex frequency
$\omega_i(t)$	exponential growth rate in time
$\omega_r(t)$	the frequency
ω_q^S	frequency from Eq. (28)

the one-dimensional solution simultaneously at all downstream locations. Hence deviations from the one-dimensional flow occurred at some locations before the arrival of the leading edge signal. This breakdown of the one-dimensional flow suggests that it may become unstable before the leading edge signal arrives. However, this breakdown has not been observed previously in numerical studies of transient flow with isothermal or constant flux boundary conditions [5,7,8]. Since no instability has been observed in numerical simulations this indicates that any instability, where it exists, must be convective rather than absolute in nature [9]. Hence, any disturbances in the numerical simulation that occur in an unstable region of the flow may not be observed because they are carried away to a stable region of the flow before their amplitude is great enough to be observed. In the experiments the natural disturbance level may be higher and hence may allow the disturbances to be observed.

Considering the initial-value problem for a small disturbance super-imposed on a parallel flow, one can find the general solution for an initial disturbance that consists of a sinusoidal input with a constant frequency at some location in space. The solution is given by the homogeneous linear stability equation with zero temporal amplification, and the frequency is given by the input forcing. This problem is known as the spatial signalling problem [9]. It is also useful in flow situations where the flow is steady but weakly non-parallel where, by making certain approximations, a spatial growth rate and wavenumber that vary slowly in space can be found. An alternative problem for a steady parallel flow is the temporal signalling problem. In this case the forcing is for only an instant in time but over the whole flow domain in a sinusoidal function in space with a constant wavelength. The solution to this problem is given by the solution to the homogeneous stability equations with zero spatial amplification and the wavelength of the input forcing [10]. In a time-dependent parallel flow, where the temporal variation is slow, the temporal signalling problem may be extended by finding a temporal growth rate and frequency that vary slowly in time.

In considering the stability of the parallel flow adjacent to a suddenly heated wall Krane and Gebhart [11] compared the frequencies observed by Joshi and Gebhart [6] to the results of a quasi-stationary linear stability analysis. They found that the experimentally observed frequencies lay above the frequency which had the maximum amplification rate predicted from their stability analysis. The use of the quasi-static assumption was cited as the probable cause for this discrepancy.

Here we examine the flow of water adjacent to a ver-

tical wall where the temperature of the wall is abruptly raised above that of its isothermal surroundings. The flow is examined experimentally, then using a full numerical simulation of the Navier–Stokes equations, and finally through linear stability analysis. The experimental setup is described in Section 2. A time series of temperature measurements at various locations within the boundary layer are taken with fast response thermistors. The numerical method is described in Section 3. Three different disturbance forcing modes are utilised in the flow simulations. Firstly a zero disturbance level is used which allows the simulation of the flow in the absence of convective instabilities. Perturbations are then introduced through continuous random heat sources throughout the boundary layer. This facilitates the comparison to the disturbance structures seen in experiments. Finally, a perturbation using a pulsed heat input at the start of the simulation with a sinusoidal structure in space is applied. This allows direct comparison to linear stability studies. The linear stability equations are described in Section 4. Stability equations using a quasi-stationary assumption are equivalent to the Orr–Sommerfeld equations (OSE) that arise by making parallel flow assumptions for a steady flow. The parabolized stability equations (PSE) are developed for a non-stationary parallel flow. These equations are analogous to the non-parallel parabolized stability equations used for stationary but spatially developing flows. The combined results are presented in Section 5 and discussed in Section 6.

2. Experimental setup

The experimental rig which models the semi-infinite plate was constructed from an existing facility previously used for experiments in a side-heated square cavity (for details of that cavity, see Patterson and Armfield [12]). Therefore, only a brief description is given here.

The cavity containing the working fluid is 24 cm wide by 31.5 cm high and 50 cm in the transverse dimension. One of the side walls of the cavity serves as the model for the semi-infinite plate. It consists of a 24×50 cm sheet of copper of thickness 1 mm, smoothly joined at its lower edge to a 7.5×50 cm sheet of PVC of thickness 1.5 cm. The leading edge, being the lower edge of a semi-finite plate, is modelled by the smooth joint between the copper and the perspex sheets. Adjacent to the copper wall is a large reservoir containing heated water. This reservoir is separated from the copper wall by a moveable gate, leaving an air gap between the gate and the copper plate. On initiation, the gate is raised pneumatically, so that the heated fluid floods against the copper wall. The conduction timescale for the copper wall is less than 10 ms, much shorter than the setup time for the thermal boundary layer. Hence, the desired step change in the thermal boundary condition is well approximated. The water in the reservoir is stirred vigorously by immersion heaters which ensures that the reservoir remains well mixed and that the temperature distribution along the plate remains almost constant in time and in spatial distribution. Through the additional use of an immersion cooler, the temperature in the reservoir is held constant to about $\pm 0.1^{\circ}$C. However, small fluctuations in the thermal boundary condition are still present.

Inside the boundary layer adjacent to the copper plate, the temperature fluctuations are measured by using fast response thermistors. These thermistors have a response time better than 7 ms and are inserted into the fluid at different locations. For the measurements discussed here, they were located at heights above the leading edge and distance away from the copper wall of (11.75, 0.2 cm), (13.95, 0.3 cm) and (16.65, 0.3 cm), respectively. Their resolution is about ± 0.006 K. The temperature of the copper wall itself was measured by three flat thermistors that were directly attached to the outside of the plate. Some of the measurements are discussed and compared to the numerical simulations in Section 5 below.

3. Numerical analysis

The flow configuration is a square cavity of height H. The initial temperature, T^* within the cavity is uniform and equal to T_0 and the vertical and horizontal velocities, u^* and v^*, are zero. The flow is initiated by raising the temperature of the left-hand-side wall to T_h at time $t^*=0$. The right-hand-side wall is maintained at T_0 and the top and bottom walls have adiabatic thermal conditions. The equations solved are the two-dimensional Navier–Stokes and energy equations with the Boussinesq approximations,

$$\frac{\partial u^*}{\partial x^*} + \frac{\partial v^*}{\partial y^*} = 0, \tag{1}$$

$$\frac{\partial u^*}{\partial t^*} + u^*\frac{\partial u^*}{\partial x^*} + v^*\frac{\partial u^*}{\partial y^*} = -\frac{1}{\rho}\frac{\partial p^*}{\partial x^*} + \nu\left(\frac{\partial^2 u^*}{\partial x^{*2}} + \frac{\partial^2 u^*}{\partial y^{*2}}\right) + g\beta(T^* - T_0), \tag{2}$$

$$\frac{\partial v^*}{\partial t^*} + u^*\frac{\partial v^*}{\partial x^*} + v^*\frac{\partial v^*}{\partial y^*} = -\frac{1}{\rho}\frac{\partial p^*}{\partial y^*} + \nu\left(\frac{\partial^2 v^*}{\partial x^{*2}} + \frac{\partial^2 v^*}{\partial y^{*2}}\right), \tag{3}$$

$$\frac{\partial T^*}{\partial t^*} + u^*\frac{\partial T^*}{\partial x^*} + v^*\frac{\partial T^*}{\partial y^*} = \kappa\left(\frac{\partial^2 T^*}{\partial x^{*2}} + \frac{\partial^2 T^*}{\partial y^{*2}}\right) + S^*, \quad (4)$$

where the origin of the coordinate system is at the base of the hot wall, and x^* and y^* are the vertical and horizontal ordinates, respectively. Here, ν is the kinematic viscosity, g the acceleration due to gravity, β the coefficient of thermal expansion and κ the thermal diffusivity. Using the length, velocity and temperature scales H, ν/H and $\Delta T = T_h - T_0$, respectively, the two non-dimensional parameters, the Rayleigh number, $Ra \equiv g\beta\Delta T H^3/\nu\kappa$ and the Prandtl number $Pr \equiv \nu/\kappa$ arise and the non-dimensional co-ordinates are given by $x_c = x^*/H$, $y_c = y^*/H$ and $t_c = t^* H^2/\nu$. The heat source term S^* is zero except when artificial perturbations are introduced. The applicability of the two-dimensional code to the cavity flow has also been recently explored by Schöpf et al. [15] where the numerical calculations were compared to shadowgraph images of a similar flow.

The non-dimensionalised Navier–Stokes equations are solved numerically using an implicit second-order time integration and a finite volume spatial discretisation on a non-staggered mesh. The procedure is that described by Patterson and Armfield [12] with further details provided in [13] and [14]. Grid refinement tests were used to ensure the solutions were converging to grid and timestep independent results. The calculations displayed were obtained using a 174 by 174 grid discretisation and time step of $\Delta t^* = 5 \times 10^{-7} H^2/\nu$. A stretched grid ensured that the vertical boundary layer received the highest resolution and the Rayleigh number $Ra = 5 \times 10^9$ and Prandtl number $Pr = 7$ are used.

4. Stability analysis

4.1. The basic flow

The transient behaviour of the fluid before it is affected by the leading edge can be modelled as if the plate were doubly infinite. In this case there is no vertical dependency in the flow and the horizontal velocity is zero. The continuity equation is trivially satisfied and the governing Eqs. (1)–(4) are reduced to,

$$\frac{\partial u^*}{\partial t^*} = \nu\frac{\partial^2 u^*}{\partial y^{*2}} + g\beta(T^* - T_0), \quad (5)$$

$$\frac{\partial T^*}{\partial t^*} = \kappa\frac{\partial^2 T^*}{\partial y^{*2}}. \quad (6)$$

For an isothermal wall boundary condition, these equations were first solved by Illingworth [16] and various solutions for uniform flux and mixed boundary condition are summarised from a number of sources in Goldstein and Briggs [3]. For the case of an isothermal boundary condition, the solution is given in terms of $\eta = y^*/\sqrt{4\kappa t^*}$,

$$T^* = T_0 + (T_h - T_0)\operatorname{erfc}\eta, \quad (7)$$

$$u^* = \frac{4g\beta\Delta T t^*}{1 - Pr}(\mathrm{i}^2\operatorname{erfc}\eta - \mathrm{i}^2\operatorname{erfc}(\eta/Pr^{1/2})). \quad (8)$$

The baseflow solutions can be non-dimensionalised by the boundary layer thickness and the maximum velocity in the boundary layer at a time $t^* = t_0$,

$$\delta = \sqrt{4\kappa t_0}, \quad U_0 = g\beta\Delta T\delta^2/\nu.$$

The non-dimensional solutions are given by,

$$\bar{u} = u^*/U_0 = \frac{Pr}{1 - Pr}(\mathrm{i}^2\operatorname{erfc}(y) - \mathrm{i}^2\operatorname{erfc}(y/Pr^{1/2})), \quad (9)$$

$$\bar{T} = (T^* - T_0)/\Delta T = \operatorname{erfc}(y), \quad (10)$$

where $y = y^*/\delta$.

4.2. The stability equations

The parabolized stability equations are developed for a parallel but time-dependent buoyancy driven boundary layer flow adjacent to a heated vertical wall. Solutions are sought to the linear stability equations with baseflow streamfunction and temperature fields $(\bar{\psi}(y, t), \bar{T}(y, t))$ and perturbations $(\psi'(x, y, t), T'(x, y, t))$,

$$\psi'_{xxt} + \psi'_{yyt} + \psi'_y\bar{\psi}_{xxx} - \psi'_x\bar{\psi}_{xxy} + \psi'_y\bar{\psi}_{yyx} - \psi'_x\bar{\psi}_{yyy} + \psi'_{xxx}\bar{\psi}_y - \psi'_{xxy}\bar{\psi}_x + \psi'_{yyx}\bar{\psi}_y - \psi'_{yyy}\bar{\psi}_x = \frac{1}{Gr_t}(T'_y - \nabla^4\psi'), \quad (11)$$

$$T'_t + T'_x\bar{\psi}_y + \bar{T}_x\psi'_y - T'_y\bar{\psi}_x - \bar{T}'_y\psi'_x = \frac{1}{Gr_t\,Pr}(T'_{xx} + T'_{yy}), \quad (12)$$

in which the equations have been non-dimensionalised by the velocity, length and temperature scales, U_0, δ and ΔT, respectively. The non-dimensional Grashof number is defined by $Gr_t = U_0\delta/\nu = g\beta\Delta T\delta^3/\nu^2$. Solutions for the perturbations (ψ', T') of the form,

$$\psi'(x,y,t) = \hat{\psi}(y,t)\exp i\left(kx - \int_{t_0}^{t}\hat{\omega}(\tau)\,\mathrm{d}\tau\right) + \text{c.c.}, \tag{13}$$

$$T'(x,y,t) = \hat{T}(y,t)\exp i\left(kx - \int_{t_0}^{t}\hat{\omega}(\tau)\,\mathrm{d}\tau\right) + \text{c.c.}, \tag{14}$$

are sought where c.c. stands for the complex conjugate and t_0 is a time after the initiation of the flow at which the analysis is performed. The perturbation is a temporally evolving wave with real wavenumber k. The first part of the perturbation is a complex eigenfunction ($\hat{\psi}(y,t)$, $\hat{T}(y,t)$) that describes the variation of the waveform in the cross-stream direction and in time. The other part of the perturbation is an exponential that describes the wave-like nature of the disturbance with $\omega_i(t)$, the imaginary part of $\hat{\omega}(t)$, being the exponential growth rate in time and the real part of $\hat{\omega}(t)$, $\omega_r(t)$, being the frequency. By analogy to the formulation for the steady non-parallel flow, the PSE are then formulated from the perturbation Eqs. (11) and (12) by neglecting all the baseflow and perturbation eigenfunction terms with second- and higher-order t derivatives, as well as multiples of terms each with first- or higher-order t derivatives. Justification for neglecting the higher order derivatives of the baseflow is based on these terms being order $O(Gr_t^{-2})$. The baseflow given by Eqs. (7) and (8) obeys this criterion. Neglecting the eigenfunction derivatives assumes that these terms are also in order $O(Gr_t^{-2})$ and is based on experience with non-parallel flows which suggests that the eigenfunctions behave in a similar fashion to the baseflow [17]. Applying these assumptions to the perturbation forms (13) and (14), the time derivative of the perturbation can be written as

$$\frac{\partial\psi'}{\partial t} = \left[(-i\hat{\omega})\hat{\psi} + \frac{\partial\hat{\psi}}{\partial t}\right]\exp i\left(kx - \int_{t_0}^{t}\hat{\omega}(\tau)\,\mathrm{d}\tau\right) + \text{c.c.} \tag{15}$$

$$\frac{\partial T'}{\partial t} = \left[(-i\hat{\omega})\hat{T} + \frac{\partial\hat{T}}{\partial t}\right]\exp i\left(kx - \int_{t_0}^{t}\hat{\omega}(\tau)\,\mathrm{d}\tau\right) + \text{c.c.}. \tag{16}$$

Substituting the perturbation forms (15) and (16) into the perturbation Eqs. (11) and (12) gives the non-stationary form of the PSE

$$L_{0,1}\hat{\psi}L_{0,2}\hat{T} + L_{2,1}\frac{\partial\hat{\psi}}{\partial t} = 0, \tag{17}$$

$$M_{0,1}\hat{\psi} + M_{0,2}\hat{T} + M_{2,2}\frac{\partial\hat{T}}{\partial t} = 0 \tag{18}$$

with the differential operators

$$L_{0,1} = -\frac{1}{Gr_t}(D^2-k^2)^2 + (\bar{\psi}_y ik - i\hat{\omega})(D^2-k^2) - \bar{\psi}_{yyy}ik,$$

$$L_{0,2} = -\frac{1}{Gr_t}D, \quad L_{2,1} = D^2 - k^2,$$

$$M_{0,1} = -\bar{T}_y ik,$$

$$M_{0,2} = -\frac{1}{Gr_t\,Pr}(D^2-k^2) - i\hat{\omega} + \bar{\psi}_y ik,$$

$$M_{2,2} = 1,$$

in which D refers to differentiation with respect to y.

A local solution procedure is used to solve Eqs. (17) and (18) with the baseflow and the perturbation eigenfunction being written as Taylor series expansions about the time t_0. The assumption of a slow time variation in the baseflow and perturbation made by the PSE ensures that all but the first two terms in the expansion can be neglected. A normalisation condition, $\hat{\omega}(t)$ is constant, is used by analogy to the normalisation condition used to derive the local PSE by Bertolotti et al. [17] for a non-parallel boundary layer. This method has also been used to successfully describe the non-parallel stability in natural convection flows by Brooker et al. [18]. The expansion of the perturbation eigenfunction is now written

$$\hat{\psi}(y,t) = \hat{\psi}_0(y) + (t-t_0)\hat{\psi}_1(y), \tag{19}$$

$$\hat{T}(y,t) = \hat{T}_0(y) + (t-t_0)\hat{T}_1(y), \tag{20}$$

and the baseflow

$$\bar{\psi}(y,t) = \bar{\psi}(y,t_0) + (t-t_0)\bar{\psi}_t(y,t_0), \tag{21}$$

$$\bar{T}(y,t) = \bar{T}(y,t_0) + (t-t_0)\bar{T}_t(y,t_0). \tag{22}$$

Substituting these into Eqs. (17) and (18) gives the local PSE

$$L_{0,1}\hat{\psi}_0 + L_{0,2}\hat{T}_0 + L_{2,1}\hat{\psi}_1 = 0, \tag{23}$$

$$M_{0,1}\hat{\psi}_0 + M_{0,2}\hat{T}_0 + M_{2,2}\hat{T}_1 = 0, \tag{24}$$

$$L_{0,1}\hat{\psi}_1 + L_{0,2}\hat{T}_1 + L_{4,1}\hat{\psi}_0 = 0, \tag{25}$$

$$M_{0,1}\hat{\psi}_1 + M_{0,2}\hat{T}_1 + M_{4,1}\hat{\psi}_0 + M_{4,2}\hat{T}_0 = 0. \tag{26}$$

The additional differential operators are

$$L_{4,1} = \bar{\psi}_{yt}(ikD^2 - ik^3) - \bar{\psi}_{yyyt}ik,$$

$$M_{4,1} = -\bar{T}_{yt}ik, \quad M_{4,2} = \bar{\psi}_{yt}ik.$$

The baseflow fields ($\bar{\psi}$, $\bar{T}$) are evaluated at $t^* = t_0$ and, given appropriate boundary conditions determined by the particular baseflow under consideration, the eigenvalue problem can then be solved.

Since the perturbation is divided into two functions, both containing t, a plane wave solution with a straight-forward definition of the frequency and temporal amplification as the gradient of the phase does not exist. The value for $\hat{\omega}$ represents only one component of the physical amplification and frequency, defined respectively as the real and imaginary parts of the downstream gradient of the perturbation, normalised by the perturbation. The physical frequency and amplification are the sum of two components, one arising from the exponential term and the other from the time dependence in the eigenfunction. Using the non-stationary formulation, the temporal amplification a_q^s and frequency ω_q^s at a time t_0 and for a flow variable q are defined by

$$a_q^s(y, t_0) = \omega_i(t_0) + Re\left(\frac{\hat{q}_1(y, t_0)}{\hat{q}_0(y, t_0)}\right), \tag{27}$$

$$\omega_q^s(y, t_0) = \omega_r(t_0) + \Im\left(\frac{\hat{q}_1(y, t_0)}{\hat{q}_0(y, t_0)}\right). \tag{28}$$

Clearly, the amplification and frequency depend on the component of the perturbation taken. For example, different values will result for the temperature component vs the velocity components.

The Orr–Sommerfeld equations are simply the PSE where all baseflow and perturbation terms of order $O(Gr_t^{-1})$ have been neglected,

$$L_{0,1}\hat{\psi}_0 + L_{0,2}\hat{T}_0 = 0, \tag{29}$$

$$M_{0,1}\hat{\psi}_0 + M_{0,2}\hat{T}_0 = 0. \tag{30}$$

The stability equations are subject to homogeneous boundary conditions for ψ', ψ'_y and T' on the hot wall at $y = 0$ and also at $y = \infty$. They are solved using a straightforward shooting method with orthonormalisation [19] that simultaneously solves for the eigenfunctions $\hat{\psi}_0$, $\hat{\psi}_1$, $\hat{T}_0$ and $\hat{T}_1$ and the complex eigenvalue $\hat{\omega}$, for a given wavenumber k, and time t_0.

5. Results

The results are separated into those dealing with random disturbances and those with discrete wavelength disturbances. In Section 5.1, random perturbations are examined. In the experimental situation the random perturbations are introduced through unavoidable vibrations that occur through the startup process and through inhomogeneities in the boundary conditions. In the numerical simulation the perturbations are introduced through thermal perturbations at the hot wall. The introduction of random disturbances results in the amplification of a broad range of wavenumbers in each case. The resulting disturbances to the fluid temperature field are then compared to the results of quasi-stationary linear stability analysis using the OSE. In Section 5.2 disturbances are introduced into the numerical simulation with discrete wavenumbers. The resultant wave structures are then compared to solutions of the non-stationary parabolized stability equations.

5.1. Random perturbations

To investigate the effect of perturbations to the wall boundary conditions, simulating natural disturbances present in an experimental rig, random perturbations were introduced into the governing Eqs. (1)–(4) through the heat source term S^*. Heat sources with randomly distributed amplitudes were continuously introduced into the grid cells adjacent to the wall. The heat source term S^* was non-zero in the region $0 < x_c < 1$, $0 < y_c < 1 \times 10^{-4}$, where

$$\frac{S^* H}{\nu \Delta T} = A_r R(x_i, y_j, t_k). \tag{31}$$

R is an evenly distributed random value between -1 and 1, and x_i, y_j and t_k are the discrete points in space and time. The perturbations therefore do not have a natural frequency or wavelength other than those associated with the discretisation. Fig. 1(a)–(c) shows the temperature isotherms in the region close to the wall when a perturbation with amplitude $A_r = 400$ is added to the flow. The temperature fields at the three times $t_c = 4.7 \times 10^{-5}$, $t_c = 9.4 \times 10^{-5}$ and $t_c = 14.1 \times 10^{-5}$ are shown. The corresponding temperature fields where no perturbation is added are shown in Fig. 1(d)–(f). The region of parallel isolines clearly defines the area of one-dimensional flow that is well described by the explicit solution, Eq. (7). Since the perturbation is continuously applied in the grid cells immediately adjacent to the vertical wall, the grid scale fluctuations can be

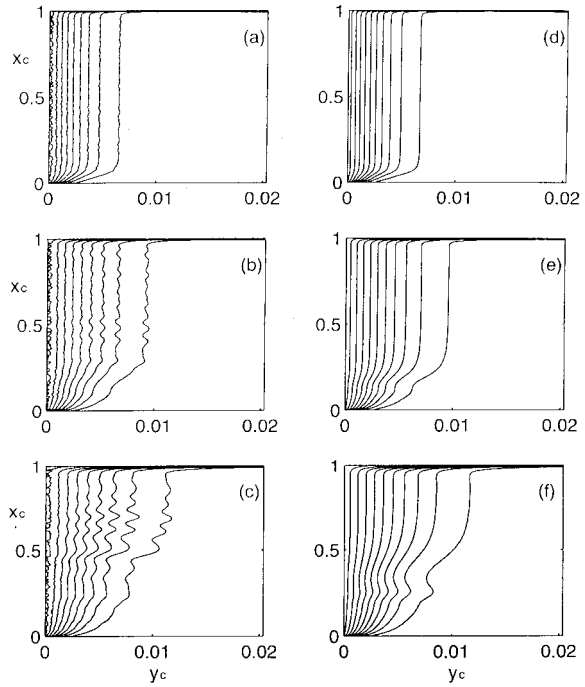

Fig. 1. Simulated temperature isolines with disturbance levels $A = 400$ in (a)–(c) and $A = 0$ in (d)–(f) at times $t_c = 4.7 \times 10^{-5}$ (a, d), $t_c = 9.4 \times 10^{-5}$ (b), (c), and $t_c = 14.1 \times 10^{-5}$ (c), (f). In each case the highest temperature isoline, $T = 0.9$, is that closest to the vertical wall, $y_c = 0$, and the subsequent isolines decrease in increments of 0.1 towards the right.

seen in the $T = 0.9$ isotherm nearest the wall. However, away from the wall the flow itself selects the disturbance wavelengths that are observed.

A time series of the temperature at a point within the flow allows an insight into the frequency response of the flow. Fig. 2 shows the simulated temperature series for both the perturbed and unperturbed flow at heights $x_c = 0.454$ and $x_c = 0.715$ and at a distance $y_c = 3.9 \times 10^{-3}$ from the wall. The unperturbed temperatures are shown by the solid lines and the perturbed temperatures by the dashed and dotted lines. The progress of the leading edge effect in the unperturbed simulation can be traced by the deviation of the temperature signal from the one-dimensional flow solution at height $x_c = 0.951$. The leading edge effect reaches the height $x_c = 0.454$ by $t_c = 0.9 \times 10^{-4}$ and the height $x_c = 0.715$ by $t_c = 1.2 \times 10^{-4}$.

We now consider the experimental results. The experiments were conducted with water as the working fluid. The mean temperature was $T_0 = 20.7°C$ giving a Prandtl number of $Pr = 6.25$. The temperature of the heated vertical side wall was maintained at 6.3°C above that of the initial temperature corresponding to a Rayleigh number of 1.6×10^9. In Fig. 3(a)–(c) a selection of

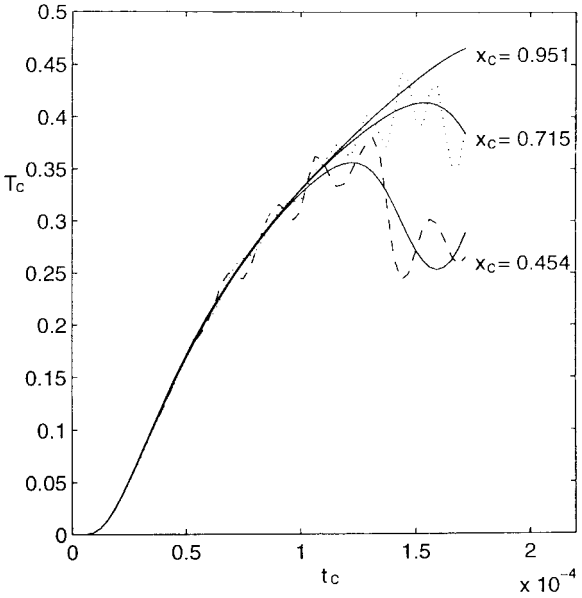

Fig. 2. The temperature at $y_c = 3.9 \times 10^{-3}$ and heights $x_c = 0.454$, $x_c = 0.715$ and $x_c = 0.951$ in an unperturbed simulation (solid lines) and at $x_c = 0.454$ (dashed line) and $x_c = 0.715$ (dotted line) in a perturbed simulation.

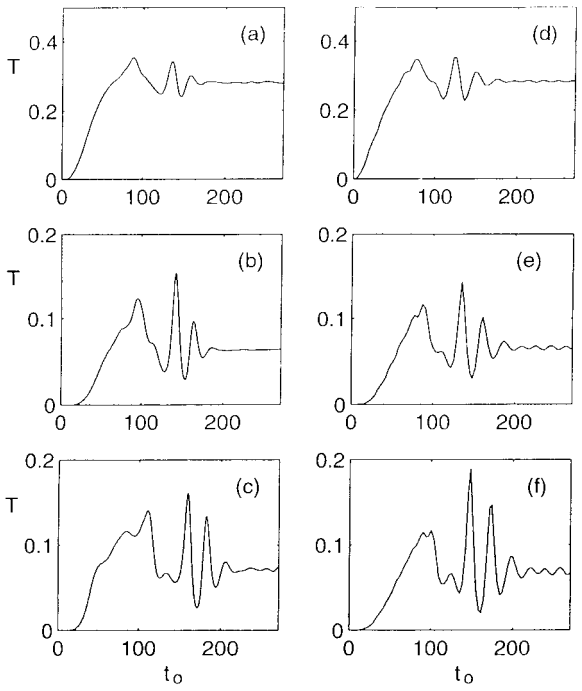

Fig. 3. Thermistor temperature measurement at locations (x^*, y^*) (a) (11.75, 0.2 cm), (b) (13.95, 0.3 cm) and (c) (16.65, 0.3 cm) as a function of time t_0. The temperatures from a perturbed numerical simulation at the equivalent locations (x_c, y_c) in a $Ra = 5 \times 10^9$ cavity at (d) (0.34, 5×10^{-3}), (e) (0.40, 9×10^{-3}) and (f) (0.48, 9×10^{-3}).

thermistor temperature measurements are shown. The thermistor measurements were made at heights above the leading edge and distances out from the wall of (11.75, 0.2 cm), (13.95, 0.3 cm) and (16.65, 0.3 cm). To facilitate comparison to the numerical simulations the non-dimensional time, $t_0 = t^*((g\beta\Delta T)^2/\nu)^{1/3}$ is used.

The experimental results allow a direct comparison between the temperature signal evolving from natural disturbances with the simulation results with random disturbances. Figs. 3(d)–(f) show the temperatures calculated at equivalent locations in a perturbed cavity simulation. The perturbation amplitude $A_r = 800$ was used with $Ra = 5 \times 10^9$ and Prandtl number $Pr = 6.25$. Note that here the Prandtl number was chosen to match the experimental situation whereas the Prandtl number $Pr = 7$ is used in all other simulations. It is not required for the computational Rayleigh number to match the experiment since the one-dimensional flow regime, Eqs. (7) and (8) is not Rayleigh number dependent.

The main features of the thermistor signals are now described with reference to Fig. 3(c). The flow is essentially in the one-dimensional regime from $t_0 = 0$ to $t_0 = 70$. From $t_0 = 70$ to $t_0 = 220$ there occurs a transition region which is associated with the influence of the leading edge of the heated surface. The features of the transition regime are an overshoot maximum which occurs at $t_0 = 95$ and a following wave packet. These features have been described previously in Armfield and Patterson [20]. After $t_0 = 220$ a steady flow regime exists. These same features can be identified in the equivalent numerical simulation in Fig. 3(f). In this study the important features to note are the wave structures moving up the plate that are observed during the one-dimensional flow region and into the overshoot region. Note that in the absence of external perturbations that no oscillations are seen in these regions as shown by the solid curve at $x_c = 0.454$ in Fig. 2. Wave structures in these regions are seen in both the experiment and the perturbed numerical simulation. The disturbance level $A = 800$ has been chosen to approximately match the amplitudes of these disturbances to the experiment. Given that no effort has been made to realistically imitate the actual disturbance structure of the experiments the agreement between experiment and numerical simulation is remarkable.

The random perturbations introduced into the flow are first damped and then amplified. After some time, the more rapidly amplified wavelengths begin to dominate the response. The flow domain and time period in which the one-dimensional flow exists in the cavity simulation is only of the order of a few wavelengths and periods on the instability. This precludes an analysis of the instability waves by Fourier transform methods. However, by measuring the wavelength and period of individual waves, the range of wave properties can be ascertained. The wavenumbers observed in the numerical simulation at several times are shown as the * symbols in Fig. 4. The wavenumber k_0 is presented in the non-dimensional form $k_0 = k^*(\nu/g\beta\Delta T)^{1/3}$. The wavenumbers have been ascertained from the numerical solution at times which correspond to Grashof number values of $Gr_t = 155$, 280, 430. Several values are shown at each time referring to the values ascertained for the individual waveforms available at each time. These wavenumbers are now compared to the amplification rates for a range of wavenumbers calculated from the Orr–Sommerfeld Eqs. (29) and (30) with the baseflow given by the one-dimensional solution, Eqs. (7) and (8). The amplification rate, ω_{0i} is presented in the non-dimensional form $\omega_{0i} = -\omega_i^*((g\beta\Delta T)^2/\nu)^{1/3}$. Hence a positive ω_{0i} implies a temporal growth. The isolines of the amplification rate are shown in Fig. 4. The observed wavenumbers lie above the maximally amplified wavenumbers and at $Gr_t = 430$ the mean observed wavenumber is approximately double that of the wavenumber with the highest amplification rate determined from the OSE.

5.2. Direct stability analysis

Direct stability analysis was carried out by introducing artificial disturbances with a discrete wavenumber source at an instant in time. The stability of the flow to forcing with individual wavenumber components is then examined and the temporal signalling problem is solved completely numerically. Since the solution utilises the full Navier–Stokes and energy equations, all possible non-stationary effects are incorporated in the analysis. In this case, the heat source term S^* is non-zero in the region $0 < x_c < 1$, $0 < y_c < 2 \times 10^{-4}$ and for the first timestep $0 < t_c < 1.25 \times 10^{-7}$ where

$$\frac{S^* H}{\nu \Delta T} = A \sin\left(\frac{2\pi x_c}{\lambda_c}\right). \tag{32}$$

The amplitude of the imposed perturbation A was chosen such that the resultant wave remained almost linear. Linearity was tested by checking that the maximum amplitude of the perturbation in the boundary layer was proportional to A and the growth rates were independent of the wave amplitude. The value $A = 40$ was used in the simulations shown.

Fig. 5 shows the temperature and vertical velocity perturbation fields calculated for an input wavelength $\lambda_c = 0.1$. The perturbation fields are defined by $T(\lambda_c) - T_{1D}$ and $U(\lambda_c) - U_{1D}$, where $T(\lambda_c)$ and $U(\lambda_c)$ are the temperature and velocity fields calculated with the input wavelength λ_c, and T_{1D} and U_{1D} are the simulated fields where there is zero input disturbance. The

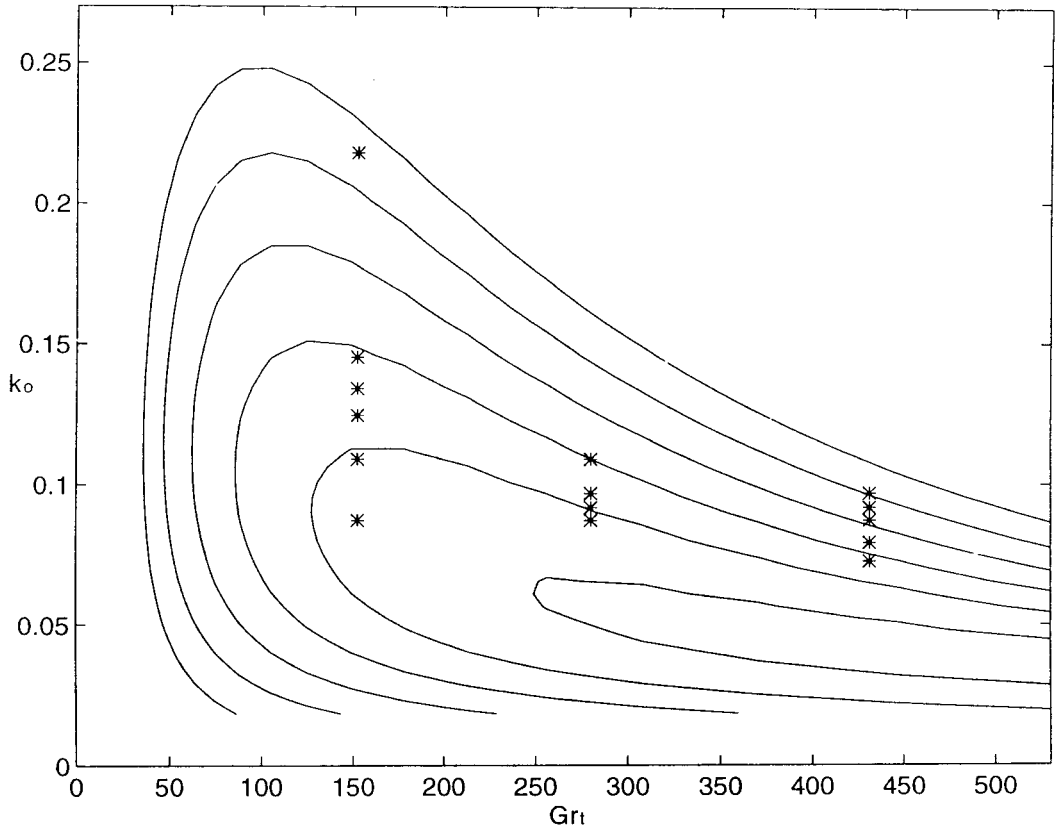

Fig. 4. Isolines of the amplification rate ω_{0i}. The * symbols indicate the wavenumbers observed in a perturbed simulation.

perturbation fields are shown at the times $t_c=2.38\times10^{-5}$, $t_c=4.62\times10^{-5}$ and $t_c=9.75\times10^{-5}$.

Since the cavity is limited by the top and bottom walls and the disturbance in the cavity can only be imposed over a finite region, the discontinuity of the input disturbance at the top and bottom walls creates wavepacket-like disturbances. The baseflow rapidly damps any disturbance once it reaches the top wall. Hence, the wavepacket emanating from the top wall is not discernible. The wavepacket emanating from the bottom discontinuity is evident in the perturbation fields. In Figs. 5(c) and (f) the wavepacket can be seen in the decay of the perturbation fields below $x_c=0.35$.

The relevant wave properties were ascertained by calculating the wave amplitudes at any given instant in time from the series of waves travelling along the one-dimensional flow. Hence the amplitude for a given flow variable q is defined as

$$A_q(y,t)=\overline{(q(x,t,t)-\overline{q(x,y,t)})^2}^{1/2} \tag{33}$$

where the overbar refers to the spatial mean over several wave periods in the vertical direction. Care was taken to ensure that the integration was carried out only over a region where the waveform is invariant in the vertical direction, thereby avoiding contamination from the wavepacket regions. The temporal amplification rate calculated from the direct stability analysis is then

$$a_q^D(y,t)=\frac{1}{A_q(y,t)}\frac{\partial}{\partial t}A_q(y,t). \tag{34}$$

The temperature and vertical velocity amplitudes A_T and A_U for the input wavelength $\lambda_c=0.1$ are shown in Fig. 6. The peak temperature amplitude decreases rapidly from time $t_c=0$ to $t_c=2.5\times10^{-5}$ after which the amplitude is relatively constant and then steadily increasing from $t_c=4.5\times10^{-5}$. The vertical velocity amplitude does not display the same rapid initial decay as the temperature signal. This is due to the disturbance being introduced into the heat equation exclusively. It is clear that some time is required for the vertical velocity perturbation to reach equilibrium with the temperature signal.

The calculation of a net amplification rate from the PSE solutions allows a comparison to the solution of the OSE. The effect of the stationary flow assumption can then be ascertained. The OSE amplification rate,

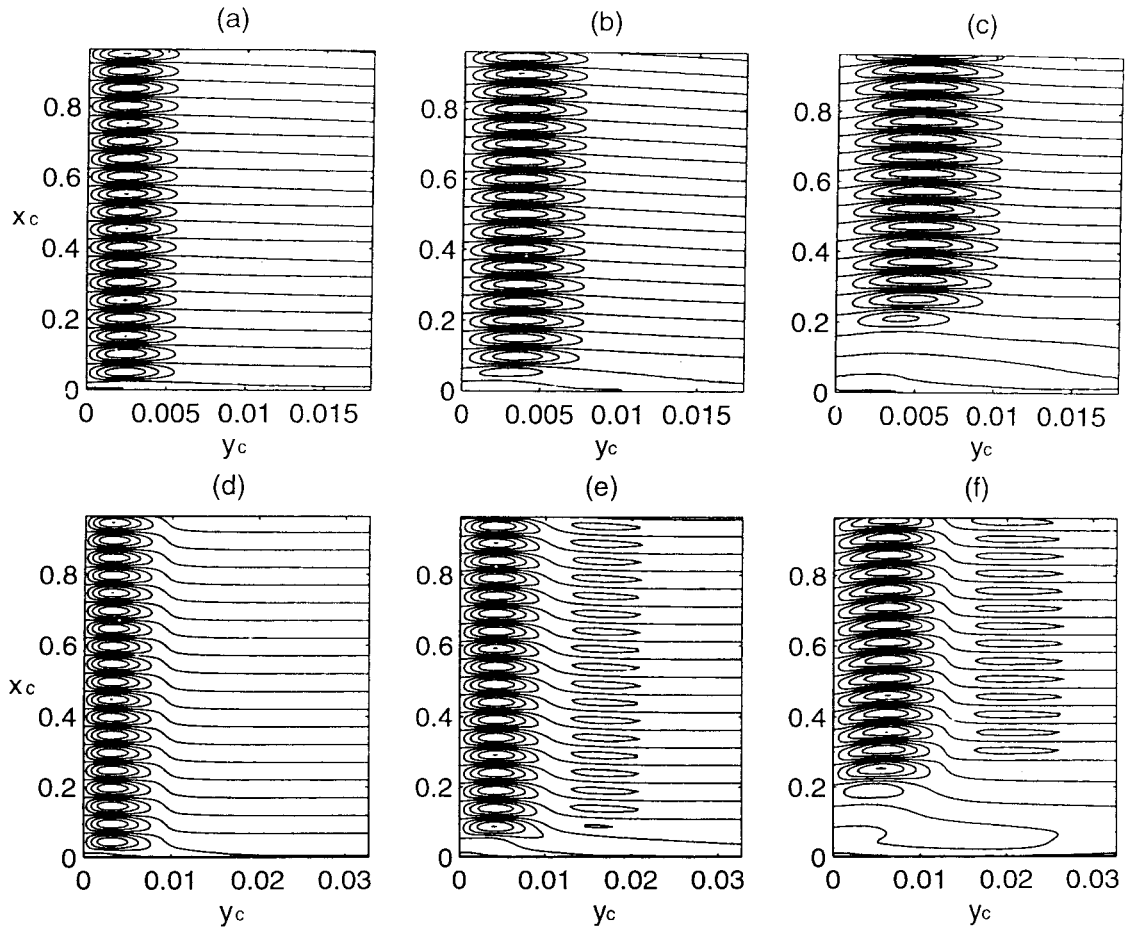

Fig. 5. The temperature perturbation fields $T(\lambda_c,\ t_c)-T_{1D}(t_c)$ for (a) $t_c=2.38\times10^{-5}$, (b) $t_c=4.62\times10^{-5}$ and (c) $t_c=9.75\times10^{-5}$ and the vertical velocity perturbation fields $U(\lambda_c,\ t_c)-U_{1D}(t_c)$ at times (d) $t_c=2.38\times10^{-5}$, (e) $t_c=4.62\times10^{-5}$ and (f) $t_c=9.75\times10^{-5}$ each for the wavelength $\lambda_c=0.1$. The contour intervals drawn in each case are: $(0,\ \pm0.25,\ \pm0.5,\ \pm0.75,\ \pm1)\times$; 1.1×10^{-3} (a); 1.2×10^{-3} (b); 4.5×10^{-3} (c); 3.8 (d); 4.1 (e); 13.5 (f).

ω_{0i}, at $Gr_t=295$ is shown by the solid curve in Fig. 7(a). The net amplification rates for the temperature a_T^s and vertical velocity a_U^s, calculated from Eq. (27) are shown by the dotted and dashed lines, respectively. The integrated amplification rates, a_U^D, and a_T^D, from direct analysis Eq. (34) are shown by the + sign for the vertical velocity by the circles for the temperature. The PSE correctly predicts that the temperature signal is amplified more rapidly than the velocity signal. It also shows that the maximally amplified wavenumber may be marginally higher than that predicted by the OSE. Fig. 7(b) shows the PSE net amplifications and the OSE amplification at $Gr_t=95$. Here the PSE temperature amplification is again higher than the vertical velocity amplification and the maximum of the temperature amplification is at a higher wavenumber.

6. Discussion

The experimentally observed oscillations that occur before the arrival of the wavepacket are qualitatively similar to those in the numerical simulations. Although some discrepancy is observed between the signals in the furthest downstream location, the spatial inhomogeneity of the disturbance level in the experiment may result in the larger amplitude in the oscillations at this height. It is also noted that the disturbance amplitude on the steady flow is higher in the simulation than in the experiment. The disturbance level in the experiment may not be homogeneous in time as it was in the simulation. In particular the experimental disturbance level is likely to be higher at the start-up of the flow caused by the method of suddenly flushing the

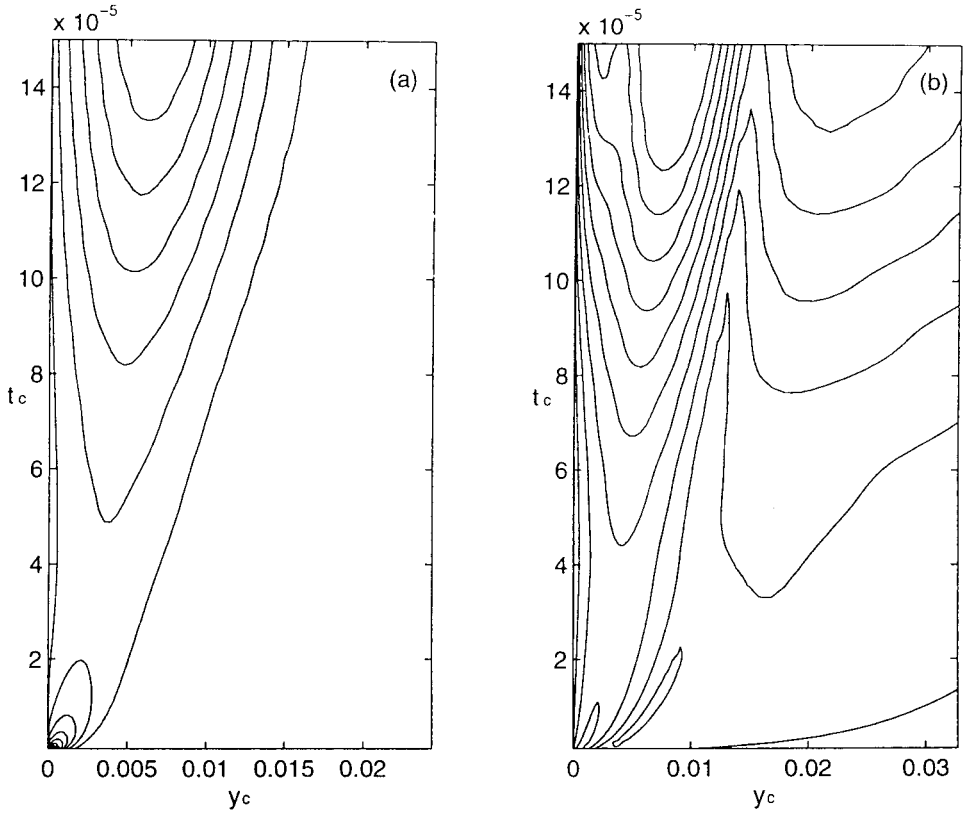

Fig. 6. (a) The temperature disturbance amplitude $A_T(y_c, t_c)$ for an input wavelength $\lambda_c = 0.1$ with contours drawn at (1, 4, 9, 16, 25, 36, 49) $\times$ 2.2×10^{-4} (b) The vertical velocity disturbance amplitude $A_U(y_c, t_c)$ for an input wavelength $\lambda_c = 0.1$ with contours drawn at (1, 4, 9, 16, 25, 36, 49) $\times$ 1.76×10^{-1}.

outside of the vertical walls to achieve an instantaneous change in wall temperature.

Direct numerical simulation of the one-dimensional flow with small random heat source perturbations has confirmed that the instability of the flow can be responsible for the breakdown of the one-dimensional flow before the arrival of the leading edge effect. The observed wavelengths resulting from random disturbances are, on average, 50% shorter than those predicted from the OSE as the most rapidly amplified. A similar trend was observed for the flux condition by Krane and Gebhart [11]. However, the comparison between the wavelength at the maximum of the amplification rate and the observed wavelength is inappropriate. The waves evolving on the one-dimensional flow from a random source can be considered as a collection of waves with all possible wavenumbers. This is different from the case for steady flows, where the evolution of natural disturbances is considered as a collection of waves with all possible frequencies. Indeed, for a parallel and temporally evolving flow, the concept of a wave with a single constant frequency is meaningless. Viewing the disturbance as a collection of waves with all possible wavenumbers, the dominant wavenumber at any given time is then given by the one with the highest amplitude at that point calculated by integrating the growth rate in time.

Assuming the amplitude of the wave at time t_0 is 1 then the logarithm of the amplitude at any time later can be calculated by integrating the amplification rate in time. The amplitude for each wavenumber is defined as e^B where

$$B(k_0, Gr_t) = \int_{Gr_{t_0}}^{Gr_t} \omega_{0i}(G)\,\mathrm{d}G,$$

and ω_{0i} is the amplification rate determined from the OSE. Since the OSE is unreliable for low Grashof numbers, the integration is carried out from $Gr_{t0} = 35$. Fig. 8 shows the isolines of B calculated using the amplification rate ω_{0i} in Fig. 4. The simulation wavenumbers are again shown by the * symbols. The maxi-

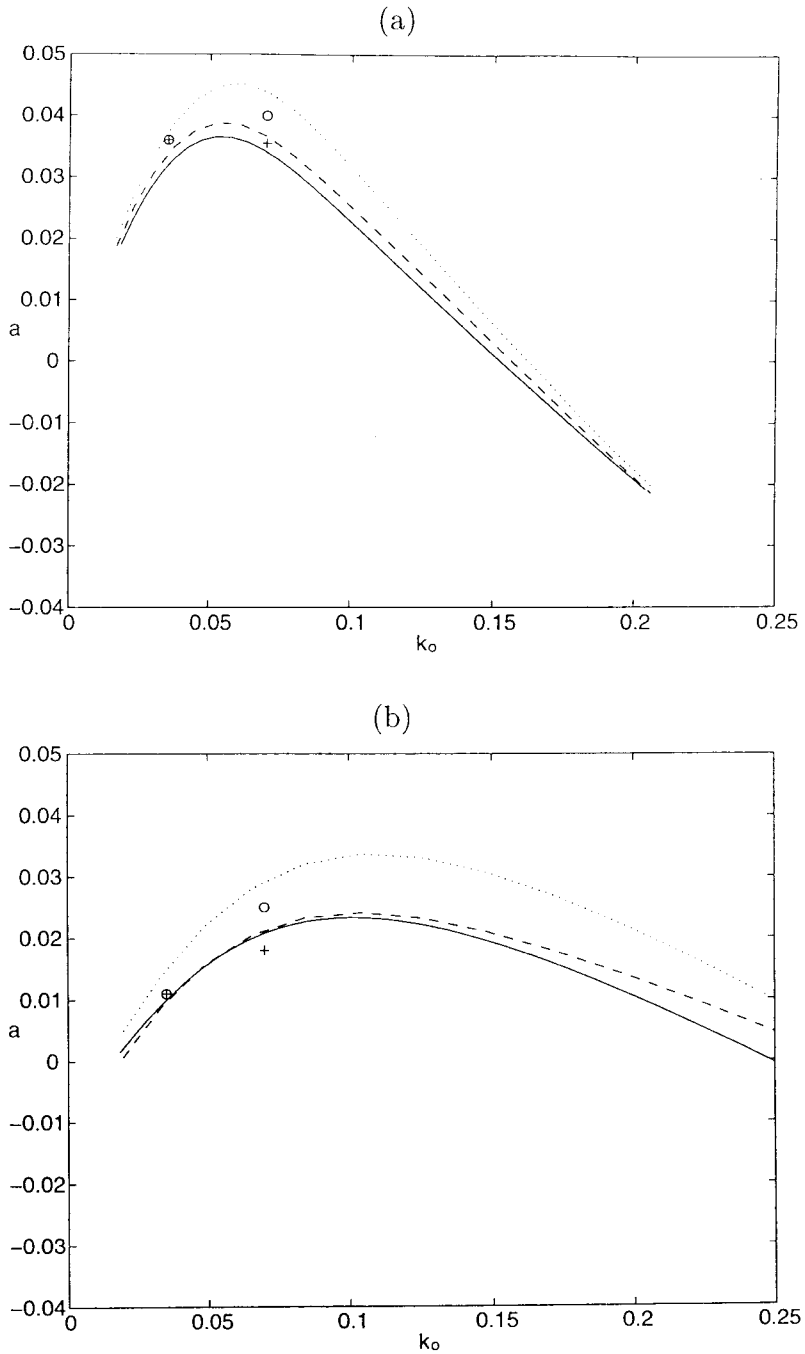

Fig. 7. The net amplification rate derived from the OSE (solid line), the PSE for the temperature signal (dotted line) and the PSE for the vertical velocity signal (dashed line) at (a) $Gr_t = 295$ and (b) $Gr_t = 95$. The circles indicate the net temperature amplification and the + signs the net vertical velocity amplification from direct analysis.

mum of the amplitude B occurs at a higher wavenumber than the wavenumber at which the maximum in the amplification rate occurs.

Fig. 9 shows the local amplification rate ω_{0i} and the amplitude B at the Grashof numbers $Gr_t = 155$, $Gr_t = 280$ and $Gr_t = 430$ as functions of the local frequency ω_{0r}. The maximally amplified frequency varies little over the times shown and is around $\omega_{0r} = 0.25$. This frequency lies well below the observed frequencies at each time depicted by the vertical dashed lines. The

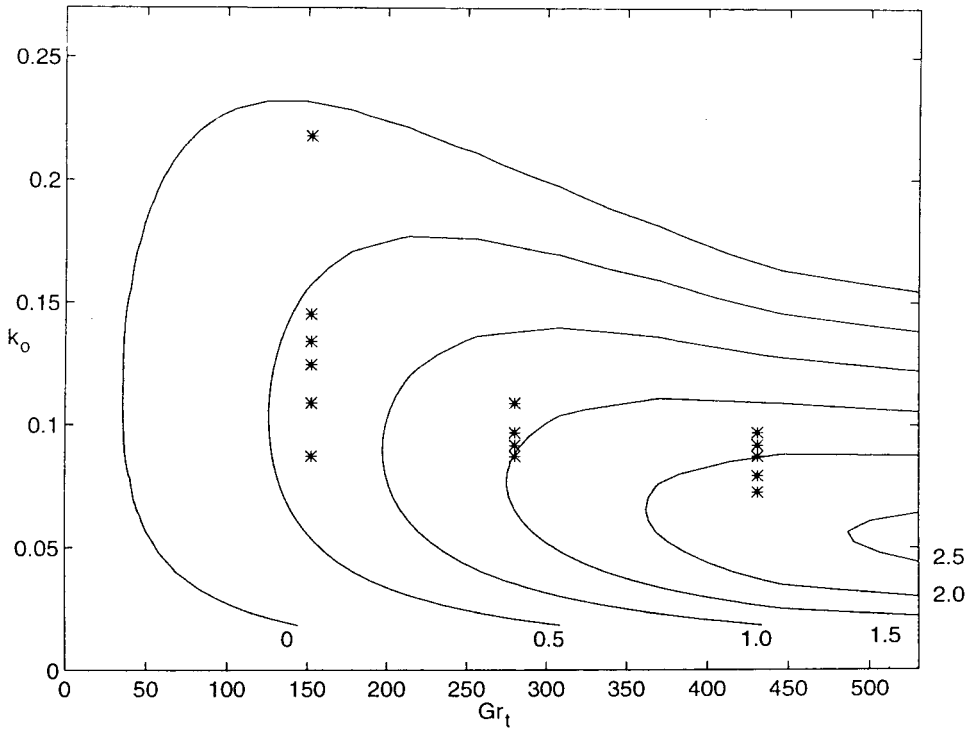

Fig. 8. Isolines of the integrated amplitude B. The * symbols indicate the wavenumbers observed in a perturbed simulation.

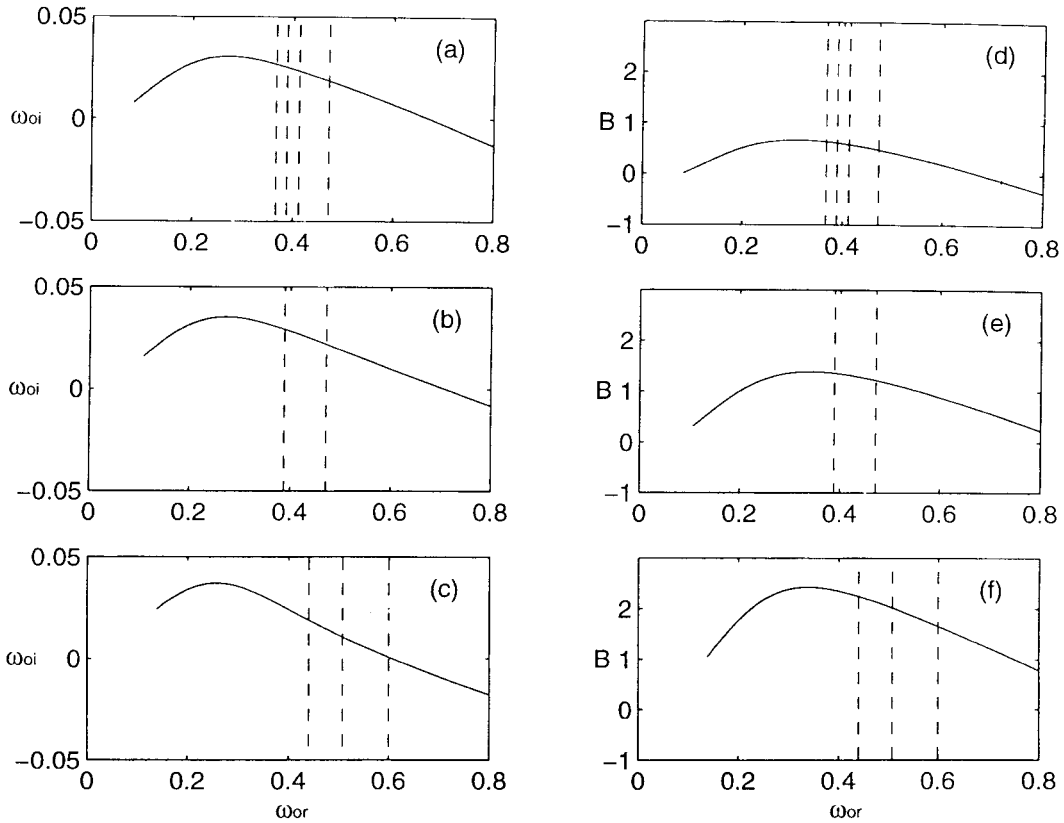

Fig. 9. (a) The amplification ω_{0i} as a function of the frequency ω_{0r} calculated from the OSE at (a) $Gr_t=155$, (b) $Gr_t=280$ and (c) $Gr_t=430$. The integrated amplitude B as a function of the frequency at (d) $Gr_t=155$, (e) $Gr_t=280$ and (f) $Gr_t=430$. The dashed lines indicate the frequencies observed in a perturbed simulation.

frequency at the maximum of the amplitude B increases slowly with time from $\omega_{0r}=0.28$ at $Gr_t=155$ to $\omega_{0r}=0.34$ at $Gr_t=430$.

The observed wavenumbers and frequencies still occur above those predicted by the maximum of the integrated amplitude. Two further factors may have influenced this result. Firstly, the rapid decay of the instability for $Gr_t < 35$ is likely to further increase the maximally amplified wavenumber. Secondly, the net amplification rate predicted using a local solution to the non-stationary PSE is greater than that by the OSE and the temperature signal is amplified at a higher rate than the vertical velocity signal. These differences are confirmed by the direct stability analysis. Hence the PSE results indicate that the non-stationary effect is to increase the amplification rate at higher wavenumbers.

Direct numerical simulation of the evolution of an instantaneous disturbance with a single discrete wavelength imposed on the one-dimensional flow has confirmed the fundamental result of the temporal signalling problem that the disturbance evolves maintaining the imposed wavelength. This direct stability analysis of the one-dimensional flow has established the feasibility of studying the stability of parallel flows by examining the temporal signalling problem. The method of direct stability analysis employed here used a heat source to initiate the disturbance. Using this source for the initial disturbance, the evolving perturbation does not attain an equilibrium between the disturbance to the temperature field and that of the momentum field until at least $Gr_t=50$. The effect of introducing the disturbance through the momentum equation or through a combination of momentum and heat sources has not been investigated but appears to be a route through which the stability properties at lower Gr_t could be obtained.

References

[1] R. Siegel, Transient free convection from a vertical flat plate, J. Heat Transfer 100 (1958) 347–359.

[2] B. Gebhart, Y. Jaluria, R.L. Mahajan, B. Sammakia (Eds.), Buoyancy-Induced Flows and Transport, Hemisphere, 1988.

[3] R.J. Goldstein, D.G. Briggs, Transient free convection about vertical plates and circular cylinders, Trans. A.S.M.E. J. Heat Transfer 86 (1964) 490–500.

[4] S.N. Brown, N. Riley, Flow past a suddenly heated vertical plate, J. Fluid Mech. 59 (1973) 225–237.

[5] S.W. Armfield, J.C. Patterson, Wave properties of natural convection boundary layers, J. Fluid Mech. 239 (1992) 195–212.

[6] Y. Joshi, B. Gebhart, Transition of transient vertical natural-convection flows in water, J. Fluid Mech. 179 (1987) 407–438.

[7] P. Le Quéré, Accurate solution to the square thermally driven cavity at high Rayleigh number, Computers Fluids 20 (1991) 29–41.

[8] S. Paolucci, D.R. Chenoweth, Transition to chaos in a differentially heated vertical cavity, J. Fluid Mech. 201 (1989) 379–410.

[9] P. Huerre, P.A. Monkewitz, Local and global instabilities in spatially developing flows, Annu. Rev. Fluid Mech. 22 (1990) 473–537.

[10] Brooker AMH (1997) Stability of the vertical natural convection boundary layer in a side-heated cavity. Ph.D. thesis, The University of Western Australia.

[11] M.J.M. Krane, B. Gebhart, The hydrodynamic stability of a one-dimensional transient buoyancy-induced flow, Int. J. Heat and Mass Transfer 36 (1993) 977–988.

[12] J.C. Patterson, S.W. Armfield, Transient features of natural convection in a cavity, J. Fluid Mech. 219 (1990) 469–497.

[13] S.W. Armfield, Finite difference solutions of the Navier–Stokes equations on staggered and non-staggered grids, Computers Fluids 20 (1991) 1–17.

[14] S.W. Armfield, Ellipticity, accuracy and convergence of the discrete Navier–Stokes equations on staggered and non-staggered grids, J. Comput. Phys. 114 (1994) 176–184.

[15] W. Schöpf, J.C. Patterson, A.M.H. Brooker, Evaluation of the shadowgraph method for the convective flow in a side-heated cavity, Experiments in Fluids 21 (1996) 331–340.

[16] C.R. Illingworth, Unsteady laminar flow of a gas near an infinite flat plate, Proc. Camb. Phil. Soc. 46 (1950) 603–613.

[17] F.P. Bertolotti, T. Herbert, P.R. Spalart, Linear and nonlinear stability of the Blasius boundary layer, J. Fluid Mech. 242 (1992) 441–474.

[18] A.M.H. Brooker, J.C. Patterson, S.W. Armfield, Non-parallel linear stability analysis of the vertical boundary layer in a differentially heated cavity, J. Fluid Mech. 352 (1997) 265–281.

[19] A. Davey, A simple numerical method for solving Orr–Sommerfeld problems, Q. J. Mech. Appl. Math. 26 (1973) 401–411.

[20] S.W. Armfield, J.C. Patterson, Direct simulation of wave interactions in unsteady natural convection in a cavity, Int. J. Heat Mass Transfer 34 (1991) 929–940.